

Selectively Nitrogen Doped ALD-IGZO TFTs with Extremely High Mobility and Reliability ¹

Dong-Gyu Kim, Hyuk Choi, Yoon-Seo Kim, Dong-Hyeon Lee, Hye-Jin Oh, Ju Hyek Lee, Junghwan Kim, Seunghee Lee, Bongjin Kuh, Taewon Kim, Hyun You Kim,* and Jin-Seong Park* ²



Cite This: ACS Appl. Mater. Interfaces 2023, 15, 31652–31663 ³



Read Online

ACCESS ⁴

Metrics & More ⁵

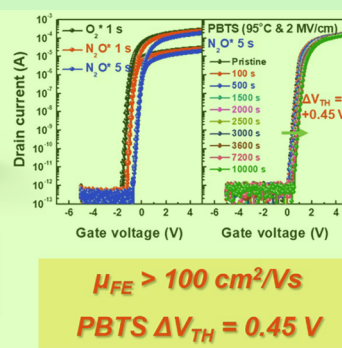
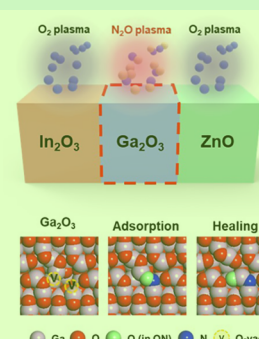
Article Recommendations

SI Supporting Information ⁷

ABSTRACT: Achieving high mobility and reliability in atomic layer deposition (ALD)-based IGZO thin-film transistors (TFTs) with an amorphous phase is vital for practical applications in relevant fields. Here, we suggest a method to effectively increase stability while maintaining high mobility by employing the selective application of nitrous oxide plasma reactant during plasma-enhanced ALD (PEALD) at 200 °C process temperature. The nitrogen-doping mechanism is highly dependent on the intrinsic carbon impurities or nature of each cation, as demonstrated by a combination of theoretical and experimental research. The Ga₂O₃ subgap states are especially dependent on plasma reactants. Based on these insights, we can obtain high-performance indium-rich PEALD-IGZO TFTs (threshold voltage:

-0.47 V; field-effect mobility: 106.5 cm²/(V s); subthreshold swing: 113.5 mV/decade; hysteresis: 0.05 V). In addition, the device shows minimal threshold voltage shifts of +0.45 and -0.10 V under harsh positive/negative bias temperature stress environments (field stress: ±2 MV/cm; temperature stress: 95 °C) after 10000 s. ⁸

KEYWORDS: atomic layer deposition (ALD), N₂O plasma reactant, nitrogen (N) doping, IGZO, oxide TFT ⁹



INTRODUCTION ¹⁰

The semiconductor industry is expanding toward artificial intelligence (AI), cloud data centers, and high-bandwidth memory processing in memory (HBM-PIM). ^{1,2} The design of high-performance field-effect transistors (FETs) with low-voltage operation, high field-effect mobility (μ_{FE}), and low leakage current has propelled the development of relevant fields. Oxide-based thin-film transistors (TFTs) are garnering increased attention owing to their steep subthreshold swing (SS) and extremely low leakage current. ^{3,4} Although oxide-based TFTs are known to restrict μ_{FE} (~30 cm²/(V s)), numerous research groups have demonstrated exceptional μ_{FE} values exceeding 100 cm²/(V s). ^{5,6}

The high stability of oxide-based TFTs is another prerequisite for their widespread application. Many groups have reported that the gate insulator (GI) plays a crucial role in determining the device stability. One crucial factor to consider is the band offset between the GI and oxide semiconductor, as it determines the energy barrier for charge carriers to move across the interface. ^{7,8} Moreover, because the GI is deposited on the active layer in the top gate structure, the stability of oxide semiconductors is highly dependent on the GI process parameters. ^{9–11} Therefore, selecting appropriate GI materials and optimizing the process parameters of the GI deposition are necessary to ensure high stability. However, achieving high

mobility and stability is challenging, as the overall properties of oxide-based TFTs are compromised. Typically, the electron mobility of oxide semiconductors (e.g., IGZO) is an apparent function of the indium cation content. The spherical 5s orbitals of indium ions generate an overlapped orbital string, increasing the IGZO band dispersion. ^{3,4,12,13} However, the oxygen vacancy (V_O) concentration increases proportionally with indium content because the dissociation energy of the indium–oxygen (3.6 ± 0.3 eV) is lower than gallium–oxygen (3.9 ± 0.2 eV). ¹⁴ Despite the high mobility of indium-rich IGZO TFTs, the increased V_O eventually destabilizes IGZO TFTs. ¹⁵

Crystalline IGZO TFTs, such as *c*-axis alignment crystalline (CAAC) and spinel phases, have been proposed for trade-off relaxation between the mobility and stability of oxide-based TFTs. ^{15–18} However, synthesizing a crystalline oxide semiconductor with large-area uniformity is technically challenging. Doping amorphous oxide semiconductors with anions may

Received: April 20, 2023

Accepted: June 8, 2023

Published: June 23, 2023



resolve the issue of uniformity. Previous studies have confirmed that nitrogen (N) doping is promising for regulating V_O defect concentration.^{11,19–21} Because the atomic radius of N is comparable to that of oxygen (O), doped N is a suitable replacement for V_O defect sites. Moreover, conventional physical vapor deposition (PVD) is already employed for high-volume manufacturing (HVM). However, limited cation controllability and an unstable chemical bonding status with anions make it challenging to achieve the device performance requirements in emerging applications. In contrast, atomic layer deposition (ALD) is an indispensable alternative capable of independently adjusting cation and anion concentrations based on repeated deposition cycles with various reactants.^{22–24} In other words, the ALD can easily determine an anion doping concentration for each element in the multicomponent oxide semiconductors by changing a reactant species.

We fabricated high-mobility IGZO TFTs capable of low-voltage operation using plasma-enhanced ALD (PEALD), and the properties of previously reported ALD-IGZO TFTs with high-mobility (<50 cm²/(V s)) are summarized in Table S1.^{25–30} Though the PEALD-synthesized IGZO channel layer is amorphous, an appropriate N-doping strategy coupled with PEALD can alleviate stability and uniformity issues. In this study, a nitrous oxide (N₂O) plasma reactant was applied selectively during each ALD cation cycle. Our strategy here, the N₂O plasma reactant, is completely different from plasma treatment in that it participates in chemical reactions during the ALD process. There have been several reports on the application of N₂O plasma reactant for insulation materials (SiO₂, Al₂O₃, HfO₂, and ZrO₂) or ZnO during PEALD, whereas IGZO multicomponent oxide semiconductor has yet to be reported clearly.^{11,31–34} Using a combinatorial study of experimental analysis and theoretical interpretation, we investigated the N-doping mechanism, and the associated enhancements in performance and stability of PEALD-synthesized IGZO TFTs were investigated. Our results provide insights into the atomic precision optimization of the performance and stability of IGZO TFTs.

EXPERIMENTAL SECTION

In₂O₃, Ga₂O₃, and ZnO Deposition by PEALD Using O₂ and N₂O Plasma Reactants. In₂O₃, Ga₂O₃, and ZnO thin films were deposited on a low-boron-doped polished silicon (Si) wafer in a 6 in. × 6 in. scale utilizing a lateral-flow-type PEALD system with a radio frequency (13.56 MHz) direct capacitance coupled plasma source (ISAC Research Inc.). The substrate temperature, working pressure, and plasma power were fixed at 200 °C, 1.2 Torr, and 100 W, respectively. During deposition, argon (Ar) (99.999%) gas was employed as the carrier gas. For In₂O₃, Ga₂O₃, and ZnO deposition, (3-(dimethylamino)propyl)dimethylindium (DADI), trimethylgallium (TMGa), and diethylzinc (DEZ) precursors were utilized. For appropriate vapor pressure, the DADI canister temperature was increased to 45 °C, whereas the TMGa was cooled to 15 °C. Additionally, the DADI precursor was delivered to a reaction chamber assisted by Ar carrier gas. To oxidize the above precursors, we utilized an aqueous O₂ or N₂O plasma diluted in Ar at a 1:1 ratio as the reactant. The O₂ and N₂O gas lines are designed to be spatially separate to minimize intermixing of the plasma species. The PEALD process steps and cycle time for these thin films are as follows: precursor dose (DADI: 1.5 s; TMGa: 0.1 s; DEZ: 0.3 s)—purge (Ar: 25 s)—reactant stabilize (O₂ and N₂O: 10 s)—plasma exposure (O₂: 1 s; N₂O: 1, 5 s)—purge (Ar: 10 s).

PEALD-IGZO Deposition via Selective N₂O Plasma Reactant. The supercycle consisting of In₂O₃, Ga₂O₃, and ZnO for IGZO

deposition was processed as [In₂O₃ × 18 cycles—Ga₂O₃ × 1 cycle—ZnO × 1 cycle]. The reference IGZO was deposited utilizing an O₂ plasma reactant, whereas selectively controlled IGZO films were deposited utilizing an N₂O plasma reactant for the individual elements In₂O₃, Ga₂O₃, and ZnO with a fixed number of subcycles. The supercycle process of the three splits of the controlled IGZO films is as follows: (i) [In₂O₃ (N₂O plasma)—Ga₂O₃ (O₂ plasma)—ZnO (O₂ plasma)], (ii) [In₂O₃ (O₂ plasma)—Ga₂O₃ (N₂O plasma)—ZnO (O₂ plasma)], and (iii) [In₂O₃ (O₂ plasma)—Ga₂O₃ (O₂ plasma)—ZnO (N₂O plasma)].

PEALD-IGZO TFTs Fabrication. Top-gate bottom-contact (TG-BC) PEALD-IGZO TFTs were fabricated on a thermally grown 100 nm thick SiO₂ buffer layer. For the source and drain electrodes, a 100 nm thick ITO layer was deposited using RF sputtering and patterned employing a conventional photolithography process. Next, a 10 nm thick reference and controlled IGZO layer deposited using PEALD was utilized as the active layer and defined by photolithography, followed by a wet etching process. As a GI, a 20 nm thick Al₂O₃ layer was deposited using PEALD, and the contact holes for the source/drain were opened. Based on the dielectric constant of PEALD-Al₂O₃ (8.05), the equivalent oxide thickness (E_{OT}) of the 20 nm thick Al₂O₃ layer was calculated as ~10 nm. To fabricate the gate electrode, a 100 nm thick ITO layer was deposited and patterned employing a conventional photolithography process. The width and length of the IGZO TFTs were 40 and 20 μm, respectively. Finally, the fabricated devices were processed postannealing at 350 °C for 3 h under dry air (O₂ 21%/N₂ 79%; purity: 99.999%) in ambient conditions.

Characterization. The electrical characteristics of the devices were measured in a dark vacuum environment at 350 mTorr by using a Keithley 4200-SCS semiconductor parameter analyzer. In addition, the electrical properties of thin films, such as the carrier concentration and resistivity, were characterized by using Hall measurements (HMS-3000, Ecopia). The cation atomic composition of the IGZO films was obtained using energy-dispersive X-ray fluorescence spectrometry (ED-XRF, ARL QUANT'X, Thermo Scientific). The chemical bond states were analyzed using X-ray photoelectron spectroscopy (XPS, K-alpha+, Thermo Scientific) employing a monochromatic Al K α (1486.6 eV) source with a pass energy of 50 eV. Crystallinity was evaluated by employing grazing incidence X-ray diffraction (GI-XRD, SmartLab, Rigaku) with a Cu K α (1.5405 Å) target. The surface morphology images and surface roughness of the IGZO films were analyzed by atomic force microscopy (AFM, XE-80, Park Systems). The amounts of quantitative N, CO, and CO₂ species were observed using thermal desorption spectroscopy (TDS, TDS1200, ESCO) from 36 to 600 °C at a rate of 60 °C/min under a high vacuum of 1 × 10⁻⁸ Pa. The thickness, subgap states near the conduction band minimum (CBM), and optical bandgap of the thin films were measured by employing spectroscopic ellipsometry (SE, M-2000, WizOptics).

First-Principles Calculations. Spin-polarized density functional theory (DFT) calculations were performed by employing the Vienna ab initio simulation package (VASP) code.^{35,36} The Perdew–Burke–Ernzerh (PBE) functional was applied to estimate the exchange-correlation energy of the Kohn–Sham equation.³⁷ The DFT-D3 method using the Becke–Johnson damping model was employed to appropriately include the van der Waals interaction.³⁸ The interaction between the ionic core and valence electrons was described utilizing the projector-augmented wave method.³⁹ The valence electron wave functions were expanded on a plane-wave basis up to an energy cutoff of 400 eV. The Hubbard-U correction method with a U_{eff} of 7 eV was applied to effectively treat the localized d-orbitals of In and Ga.^{40–43} The Brillouin zone was sampled at the Γ -point for all calculations. The convergence criteria for the electronic structure and atomic geometries are 10⁻⁴ and 0.05 eV/Å, respectively. To improve the state convergence near the Fermi level, a Gaussian smearing function with a finite temperature width of 0.05 eV was utilized. To describe the atomic structure of the ALD-synthesized films, 2 × 2 × 4 In₂O₃ (111), 3 × 2 × 5 β-Ga₂O₃ (010), and 5 × 5 × 4 ZnO (101) slab models were employed (Figure 6a). A 15 Å vacuum layer was applied to avoid interactions between the periodic supercells.

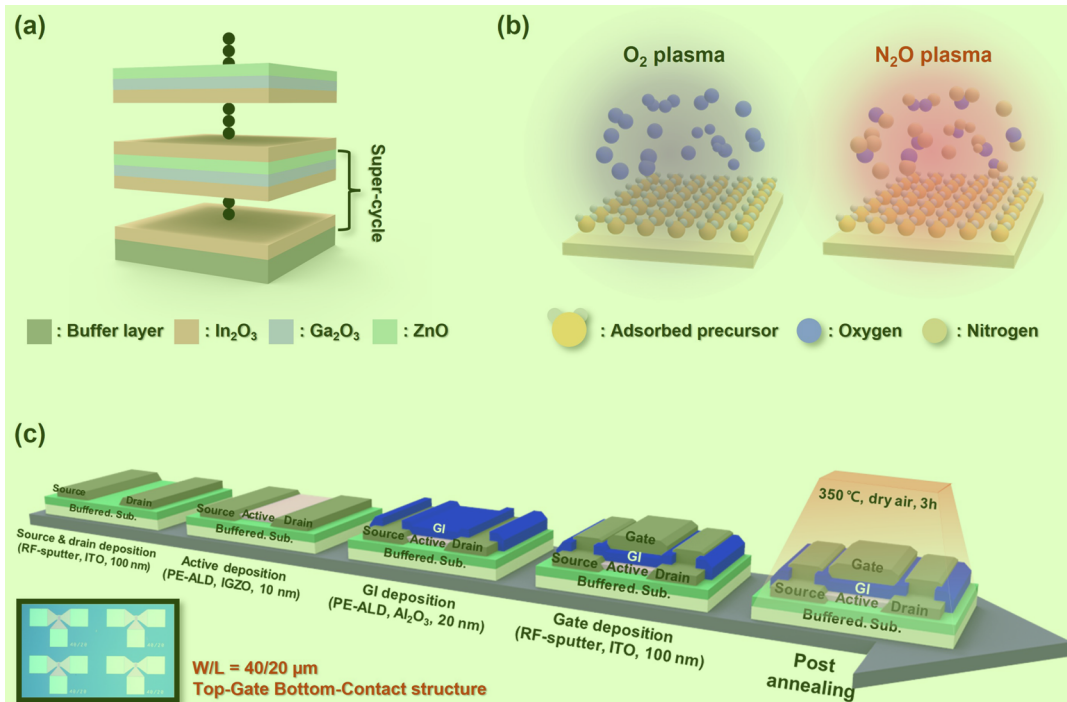


Figure 1. Deposition method of PEALD-IGZO films and device fabrication process. Schematic of (a) IGZO deposited with supercycle, (b) O₂ and N₂O plasma ignition, and (c) device fabrication process. It was confirmed that the TFT arrays were well separated using an optical microscopy image.

RESULTS AND DISCUSSION

Impact of N₂O Plasma Reactant on the Electrical Characteristics of PEALD-IGZO TFTs. PEALD-IGZO active layers were deposited on the buffer layer utilizing a supercycle method consisting of In₂O₃, Ga₂O₃, and ZnO, as depicted in Figure 1a. To clarify the effect of the plasma reactant species on the TFT characteristics, IGZO active layers were deposited using O₂ and N₂O plasma reactants, as shown in Figure 1b. Here, the plasma reactants are completely different from plasma treatment in that they participate in chemical reactions during the ALD process. As shown in Figure 1c, we fabricated TG-BC PEALD-IGZO TFTs using a conventional photolithography process, and it was also confirmed that the TFT arrays were well separated. Figure 2 shows the transfer characteristics of the PEALD-IGZO TFTs using the O₂ and N₂O plasma reactants, and the device key parameters are summarized in Table S2. The IGZO TFT with an O₂ plasma reactant exhibits an outstanding μ_{FE} of $135.8 \pm 4.1 \text{ cm}^2/(\text{V s})$, whereas it significantly deteriorates from 85.0 ± 4.4 to $23.6 \pm 0.2 \text{ cm}^2/(\text{V s})$ when the N₂O plasma reactant time increases from 1 to 5 s. Furthermore, the N₂O plasma time results in increased SS and hysteresis with a positive threshold voltage (V_{TH}) shift. Figure 2b illustrates the positive bias temperature stress (PBTS) stability results at 95 °C for 10000 s with a gate field stress of 2 MV/cm. The IGZO TFTs with the N₂O plasma reactant demonstrated poorer stability than those with the O₂ plasma reactant. These inferior electrical characteristics of the N₂O plasma reactant were investigated by using XPS. Figure 2 depicts the XPS O 1s and N 1s peaks of the IGZO thin films. Compared with the O₂ plasma reactant, the oxygen deficiency (O_{def}) peak decreased from 22.5 to 19.9% with increasing N₂O plasma time. Considering the increase in N content up to 0.2 at. % within the N₂O plasma time of 5 s, the decrease in O_{def} could be ascribed to the N-doping effect, as

described in the literature.^{11,19–21} Typically, N doping in IGZO can contribute to decreasing oxygen-related defects because its atomic radius is comparable to that of O and N. Therefore, many research groups have demonstrated promising device stability using N doping in sputtering-derived IGZO, which generally possesses an atomic composition of In:Ga:Zn = 1:1:1 at. %. Because indium-rich IGZO (Table S3) was deposited using the PEALD process herein, the puzzling poor stability of the N₂O plasma reactant implies the dependency of N doping effects on the IGZO cation composition. Considering these results, indium, gallium, and zinc cations were hypothesized to exhibit different tendencies in the N₂O plasma reactant effects.

Selective N₂O Plasma Reactant Application for Each Cation Element of PEALD-IGZO. To gain insight into the N₂O plasma reactant effects for each cation in IGZO, we fabricated three splits of IGZO films for the active channel layer. As depicted in Figure 3a, the IGZO films were deposited considering the O₂ plasma reactant, whereas indium, gallium, and zinc subcycles were selectively applied to the N₂O plasma reactant (* means N₂O plasma reactant, denoted by I*GZO, IG*ZO, and IGZ*O, hereafter). The difference in cation atomic composition of the three splits of IGZO films is negligible, as shown in Figure S1 and Table S4. Figure 3 illustrates the transfer characteristics of the I*GZO, IG*ZO, and IGZ*O TFTs. The black dots indicate the reference IGZO TFT deposited using an O₂ plasma time of 1 s, whereas the red and blue dots represent IGZO TFTs with selective N₂O plasma times of 1 and 5 s for each cation, respectively. The electrical parameters, such as V_{TH} , μ_{FE} , SS, and hysteresis, extracted from the transfer characteristics are presented in Table 1. To more clearly identify the effect of N₂O plasma reactant on electrical characteristics, the μ_{FE} values of I*GZO, IG*ZO, and IGZ*O TFTs as a function of gate voltages are

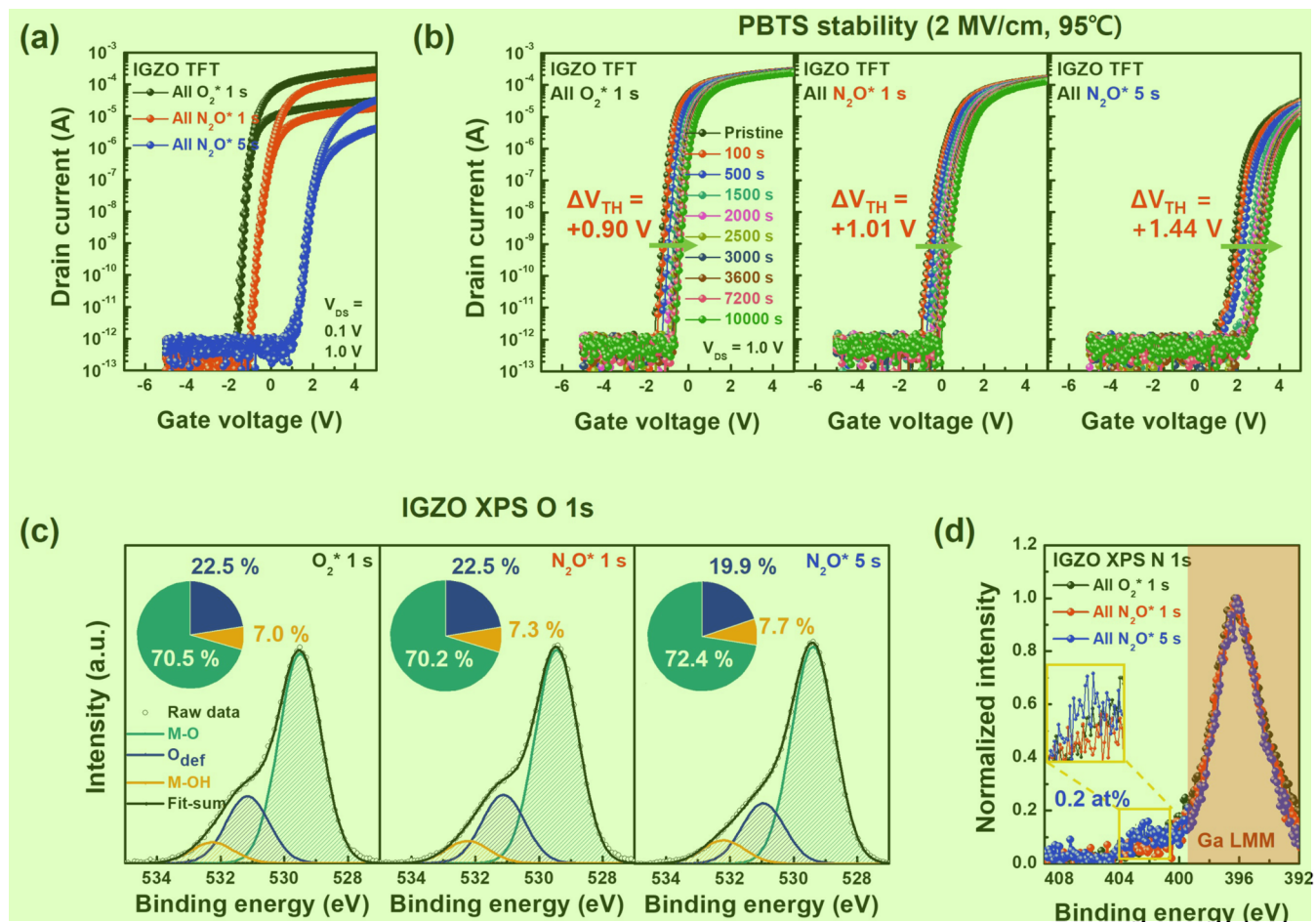


Figure 2. Comparison of electrical characteristics of the PEALD-IGZO TFTs deposited using O₂ and N₂O plasma reactants. (a) Transfer curves and (b) PBTS results of the IGZO TFTs. XPS (c) O 1s and (d) N 1s peaks of the IGZO films.

compared in Figures 3e, 3f, and 3g, respectively. The μ_{FE} and SS values degraded with a positive V_{TH} shift with an increasing N₂O plasma time for each cation material. However, the variations in the electrical parameters were slightly different depending on the cation type. In particular, the I^{*}GZO TFTs exhibited a significant decrease in μ_{FE} ($135.8 \rightarrow 23.2 \text{ cm}^2/(\text{V s})$) with an increasing N₂O plasma time. However, the N₂O plasma effects on Ga₂O₃ in IG^{*}ZO TFTs were insignificant compared with those of In₂O₃. Among the electrical parameters, the N₂O plasma for Ga₂O₃ produces IG^{*}ZO TFTs with a positive V_{TH} shift ($-1.41 \rightarrow -0.47 \text{ V}$). Furthermore, a large increment of SS ($72.3 \rightarrow 145.1 \text{ mV/decade}$) in the IGZ^{*}O TFTs was observed. Based on these experimental results, the N₂O plasma reactants for In₂O₃, Ga₂O₃, and ZnO in the IGZO system could possibly serve as mobility suppressors, V_{TH} stabilizers, and slope destroyers, respectively. To identify the unique characteristics of the N₂O plasma reactant for each cation in the IGZO TFTs, GI-XRD was performed, as depicted in Figure S2. Because the selective N₂O plasma IGZO active layers exhibited an amorphous phase, the relationship between the electrical characteristics and crystallinity was not considered. During device fabrication, the only difference between the reference and selective N₂O plasma IGZO TFTs was the plasma reactant species for each cation material. Therefore, focusing on each cationic material could reasonably explain these results with precision.

Gap States and Light Element Analysis of Each Cation Material Deposited Using N₂O Plasma Reactant.

The electrical characteristics of In₂O₃, Ga₂O₃, and ZnO prepared by using the O₂ or N₂O plasma reactants were investigated via Hall measurements. However, because of the low Ga₂O₃ carrier concentration, only the electrical characteristics of the In₂O₃ and ZnO thin films could be obtained, as depicted in Figures S3a and S3b, respectively. The In₂O₃ and ZnO films exhibited a decrease in carrier concentration and increased resistivity with the N₂O plasma time. The V_O is an important factor in determining carrier concentration and resistivity in oxide semiconductors.^{3,4,44,45} Therefore, XPS analysis of each cation material was performed to evaluate the effects of the N₂O plasma reactant on the electrical characteristics. Figure 4 illustrates a comparison of the XPS 1s peaks for the In₂O₃, Ga₂O₃, and ZnO films prepared using O₂ or N₂O plasma reactants. The O 1s peaks were deconvoluted by utilizing a Gaussian fit with three different binding energy-centered peaks, as depicted in Figure S4. It is found that negligible changes in the O_{def} peak are observed regardless of plasma species in the In₂O₃ films. In contrast, the intensity of the O_{def} peak decreased in the Ga₂O₃ and ZnO films with increasing N₂O plasma time (Ga₂O₃: 14.8 → 8.0%; ZnO: 22.5 → 17.5%). The correlation between the O_{def} and subgap states was measured via SE analysis. Figure 4 illustrates the SE spectra of In₂O₃, Ga₂O₃, and ZnO, and the inset shows the bandgap variations for each material. The band edge states

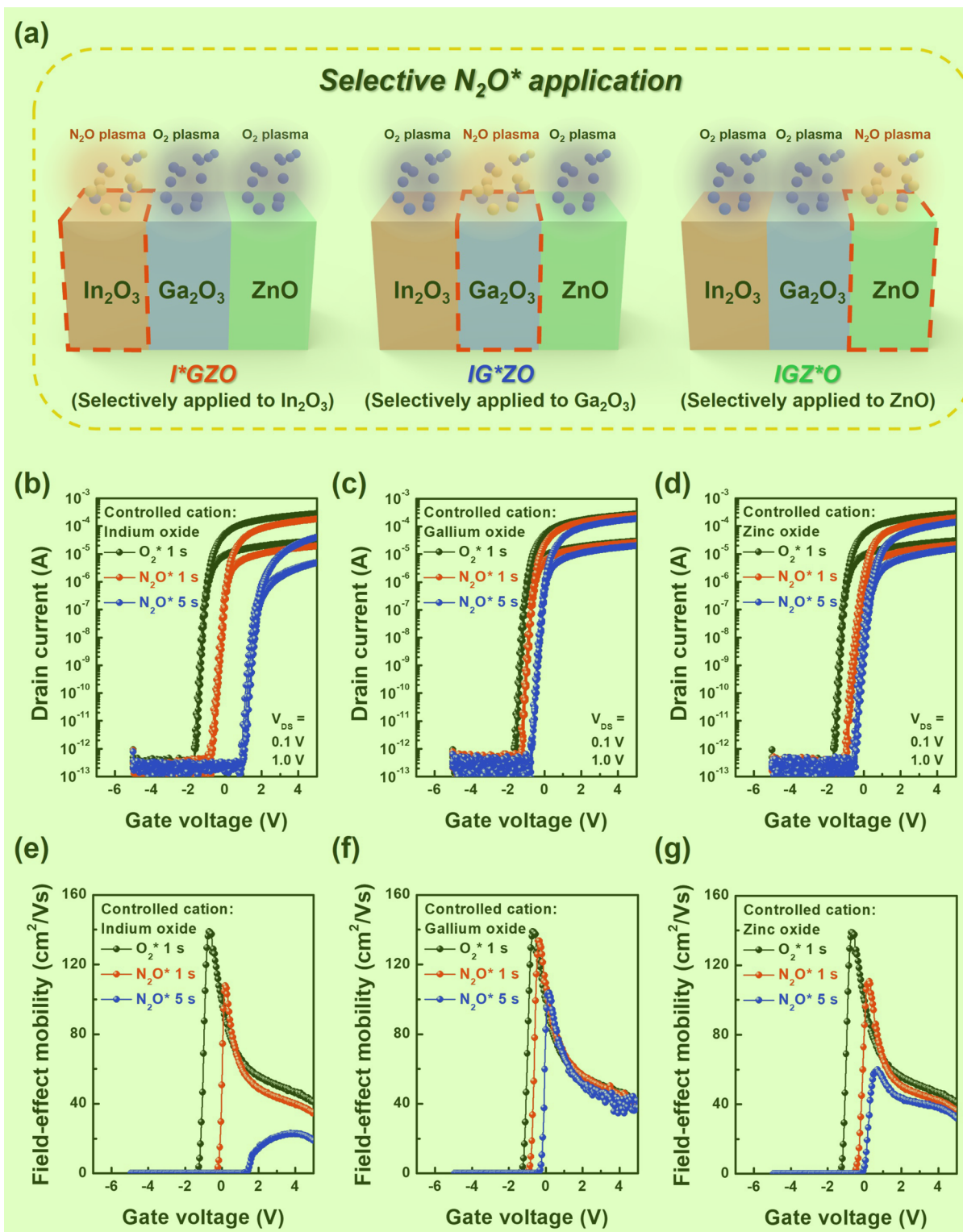


Figure 3. Electrical characteristics of the selective N_2O applied IGZO TFTs. (a) Schematic of selective N_2O plasma reactant applications in IGZO active layers. Transfer curves and extracted μ_{FE} as a function of gate voltages of the IGZO TFTs with selective N_2O plasma applied for (b, e) indium oxide, (c, f) gallium oxide, and (d, g) zinc oxide.

were deconvoluted with two Gaussian fits located at E_C -0.02 (D1 state, donor-like state) and E_C -0.27 (D2 state, acceptor-like state), as depicted in Figure S5. Based on the estimated number of subgap states, the energy structures of In_2O_3 , Ga_2O_3 , and ZnO are presented in Figures 4g, 4h, and 4i, respectively. Compared to the values for the O_2 plasma reactant, the donor level for carrier-generating In_2O_3 and ZnO

films decreased with the N_2O plasma time. Contrary to the trends for donor-level changes, the variations in the subgap states are fairly different for each cation element. The subgap states increased in the In_2O_3 film with N_2O plasma time, whereas they decreased in the Ga_2O_3 film utilizing the N_2O plasma reactant. However, the subgap states are undetected in the ZnO film regardless of the reactant species, which is

Table 1. List of Key Electrical Parameters of IGZO TFTs with Selective N₂O Plasma Reactant 1

IGZO type	plasma condition	V_{TH} (V)	μ_{FE} (cm ² /V s)	SS (mV/dec)	hysteresis (V)	2
I*GZO	O ₂ * 1 s	-1.41 ± 0.01	135.8 ± 4.1	72.3 ± 18.5	0.04 ± 0.02	
	N ₂ O* 1 s	-0.34 ± 0.07	97.0 ± 6.4	93.7 ± 23.5	0.05 ± 0.01	
	N ₂ O* 5 s	1.22 ± 0.04	23.2 ± 0.5	117.2 ± 20.5	0.15 ± 0.03	
IG*ZO	O ₂ * 1 s	-1.41 ± 0.01	135.8 ± 4.1	72.3 ± 18.5	0.04 ± 0.02	
	N ₂ O* 1 s	-0.96 ± 0.08	132.6 ± 8.6	75.8 ± 11.7	0.05 ± 0.00	
	N ₂ O* 5 s	-0.47 ± 0.02	106.5 ± 2.7	113.5 ± 29.8	0.05 ± 0.01	
IGZ*O	O ₂ * 1 s	-1.41 ± 0.01	135.8 ± 4.1	72.3 ± 18.5	0.04 ± 0.02	
	N ₂ O* 1 s	-0.68 ± 0.12	110.1 ± 8.3	145.1 ± 6.0	0.08 ± 0.02	
	N ₂ O* 5 s	-0.27 ± 0.04	62.9 ± 1.6	135.7 ± 4.9	0.11 ± 0.01	

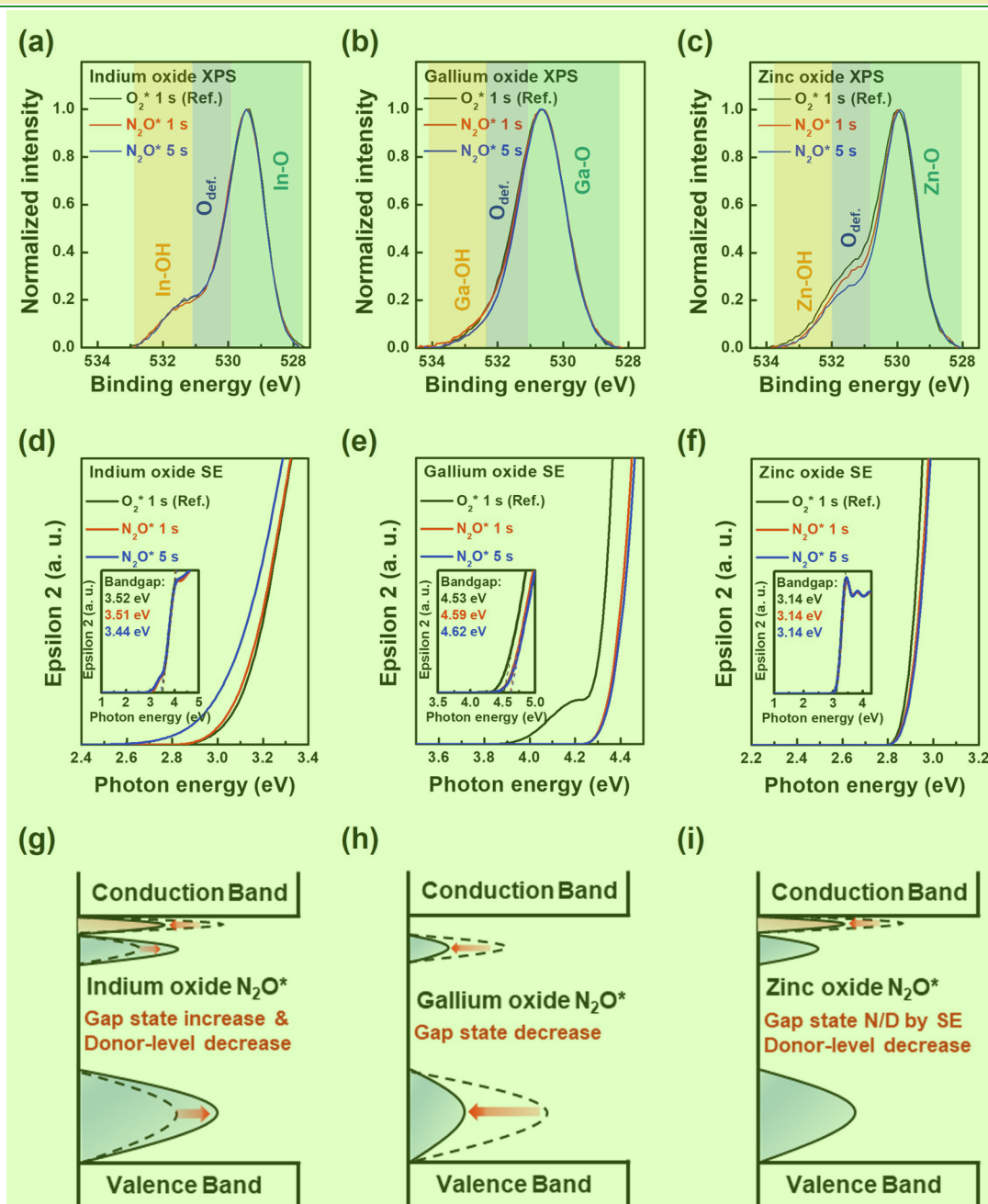


Figure 4. Differences in oxygen-related gap states by N₂O plasma reactant. XPS O 1s peaks of the (a) In₂O₃, (b) Ga₂O₃, and (c) ZnO films. SE spectra of the dielectric function (ϵ_2) and bandgap (inset) of the (d) In₂O₃, (e) Ga₂O₃, and (f) ZnO films. Schematic of the band structure of (g) In₂O₃, (h) Ga₂O₃, and (i) ZnO extracted from SE analysis. 4

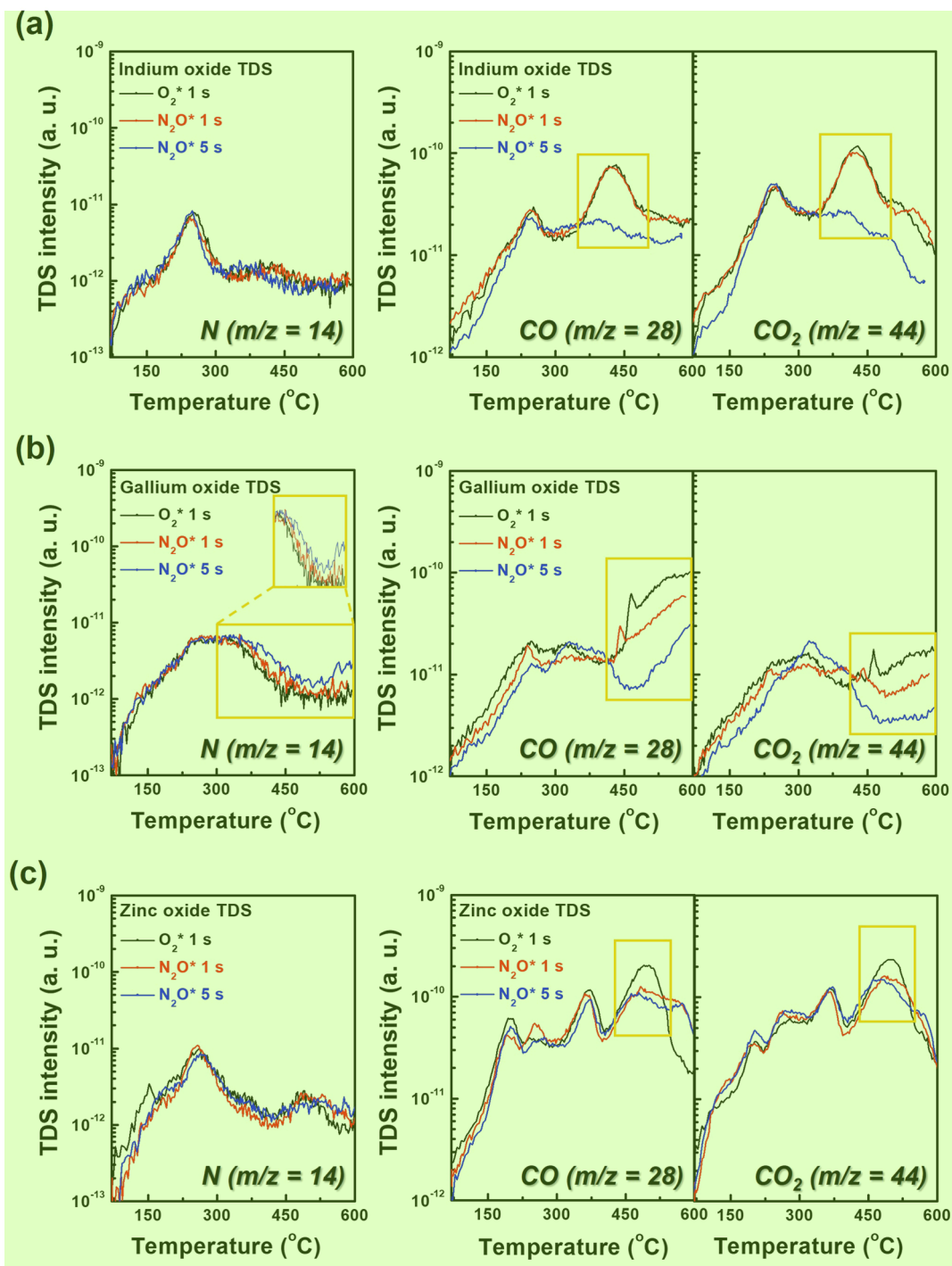


Figure 5. Desorption behaviors of the nitrogen and carbon species in the In_2O_3 , Ga_2O_3 , and ZnO films fabricated with O_2 or N_2O plasma reactant. **2** TDS spectra of the (a) In_2O_3 , (b) Ga_2O_3 , and (c) ZnO films fabricated by using an O_2 plasma exposure time of 1 s and N_2O plasma times of 1 and 5 s.

presumed to result from acceptor-like V_O^{2+} states located at a relatively deep energy level (~ 1 eV far from the CBM) or exhibited high formation energy (~ 3.5 eV).^{46–48} These results imply that the N_2O plasma reactant to In_2O_3 reduces the donor level, resulting in mobility suppression in the I*GZO TFT. However, because Ga_2O_3 has a low electron concentration, the subgap states are more sensitive to the N_2O plasma reactant than the donor level, eventually contributing to V_TH stabilization in the IG*ZO TFT. Meanwhile, the surface roughness of the IGZ*O slightly increased to other films,

which probably resulted from the N_2O plasma treatment on top of ZnO in the IGZO structure (Figure S6).^{11,49,50} Because ZnO is directly in contact with the GI, significant degradation of SS in the IGZ*O TFTs is presumed to increase in surface roughness. In addition to the consequences of the N_2O plasma reactant effect, determining the causes for the varied N_2O plasma reactant effect in In_2O_3 , Ga_2O_3 , and ZnO films is crucial.

In our experiments, IGZO films were grown by using the PEALD process, which is entirely distinct from the conven-

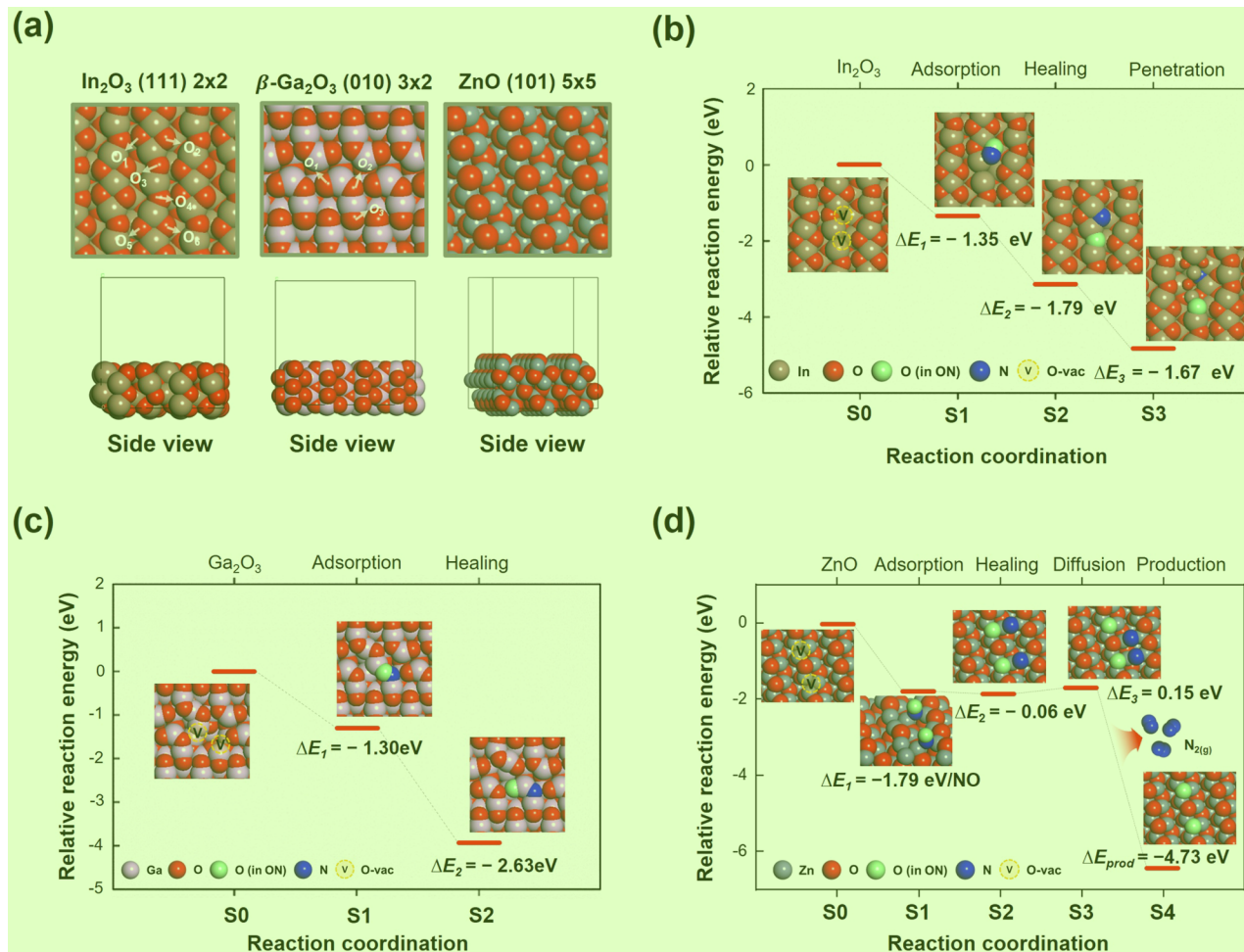


Figure 6. DFT-constructed surface models of oxide films and energetics of ON–oxide interaction. (a) Surface models of oxide films. Energetics of ON adsorption and dissociation on (b) In_2O_3 , (c) Ga_2O_3 , and (d) ZnO . The reaction energy of a single step, ΔE_n , was calculated by $\Delta E_n = E_{S_n} - E_{S_{n-1}}$.

tional sputtering process. The PEALD process is based on the following four steps: precursor dose, precursor purge, plasma reactant dose, and plasma reactant purge. Specifically, the plasma reactant dose step plays a key role in film growth because chemical reactions occur between the $\text{O}_2/\text{N}_2\text{O}$ plasma reactant and the adsorbed precursors. During O_2 and/or N_2O plasma ignition, the precursor ligands are oxidized by abundant O and/or ON radicals and are eventually purged out as CO and/or CO_2 .^{22–24} For N_2O plasma ignition, the adsorbed-ON radicals possibly retain the N content in the deposited film, leading to oxygen-related defect passivation or N-related defect creation. In addition, the limited plasma exposure time during PEALD cycles results in an incomplete chemical reaction between the precursor and oxidant, leading to residual carbon (C) impurities in the deposited films. These C impurities have been reported to act as shallow donors in oxide semiconductors.^{51,52} Therefore, examining whether N_2O plasma can affect changes in the N content and C-related impurities is valuable, which could lead to subgap states and donor-level differences. Figure 5 depicts the TDS spectra of In_2O_3 , Ga_2O_3 , and ZnO . The black, red, and blue dots represent the O_2 plasma for 1 s, N_2O plasma for 1 s, and N_2O plasma for 5 s, respectively. To observe the variations in the N content and C-related impurities, the mass/charge (m/z) ratios of 14 (N), 28 (CO), and 44 (CO_2) were examined. Notably, the N content

was detected only in Ga_2O_3 films with increasing the N_2O plasma time. Furthermore, considering that the N content is desorbed above 500 °C, N might form a strong bond with gallium ions, thereby contributing to decreasing subgap states in the Ga_2O_3 film utilizing the N_2O plasma reactant. Additionally, In_2O_3 not only has any N content but also exhibits negligible changes in the content of O_{def} , regardless of the plasma ignition conditions. Therefore, an increase in the In_2O_3 film subgap states with N_2O plasma treatment time could possibly result from the creation of oxygen-related defects (oxygen interstitial or peroxide) caused by excess N_2O plasma treatment. In contrast, C-related impurities (CO and CO_2) decreased slightly with the N_2O plasma time compared to those of the O_2 plasma reactant. Recently, Shiah et al. reported that CO-related impurities are regarded as donors in oxide semiconductors and have a greater effect on high-mobility oxide semiconductors with deep energy levels of the CBM.⁵¹ Based on this result, a decrease in the In_2O_3 donor level would reduce donor-like C impurities with increasing N_2O plasma time. However, the decrease in the ZnO donor level with N_2O plasma time is thought to predominantly originate from the decrease in O_{def} than that of the CO-related impurities because ZnO mobility is generally much lower than that of In_2O_3 . Additionally, for an in-depth study of the behavior of N- and C-related species in the N_2O plasma

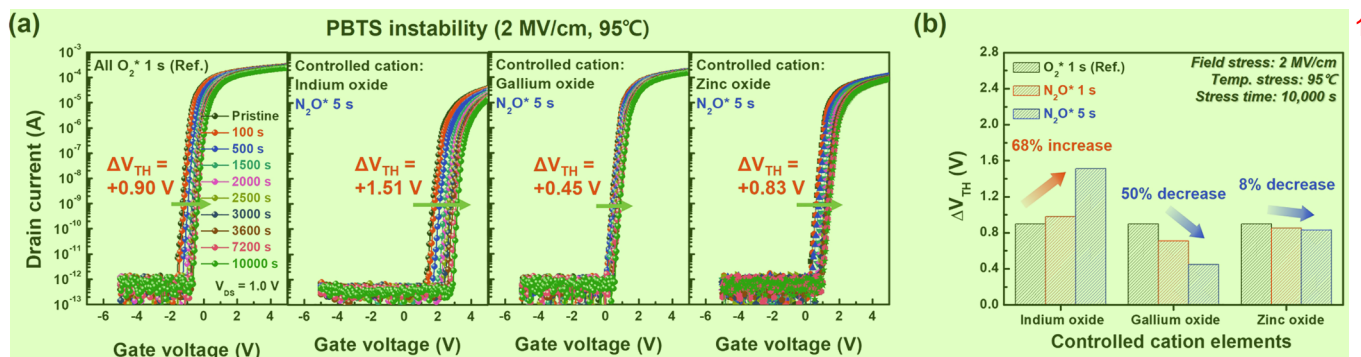


Figure 7. PBTS stability of the selective N₂O applied IGZO TFTs. (a) Transfer curves as a function of PBTS time of the reference and selectively N₂O plasma applied IGZO TFTs. (b) Degree of V_{TH} shift after 10000 s of PBTS time for IGZO TFTs.

reactant, the TDS spectra for In₂O₃, Ga₂O₃, and ZnO films were analyzed for deliberate enhancements of ON radical adsorption (N₂O plasma time of 10 s), as illustrated in Figure S7. Compared to the N₂O plasma times of 1 and 5 s, the N content evidently increased with a significant decrease in C-related impurities in the In₂O₃ film prepared using a N₂O plasma time of 10 s. This result implies that the N content in the In₂O₃ film is closely related to the C-related impurities. For the Ga₂O₃ film, the N content increased for the N₂O plasma time of 10 s, whereas the C species were comparable to those for the N₂O plasma for 5 s. Because the lowest limit of the C-related impurities was observed for the N₂O plasma time of 5 s, the increased N content for the N₂O plasma for 10 s could be attributed to the increased frequency of the ON radical adsorption. However, any N content in the ZnO film was undetected even when fabricated using a N₂O plasma time of 10 s, whereas the C-related species evidently decreased with a N₂O plasma time. The ZnO film was devoid of N, regardless of C impurities. Despite the changes in the C and N contents in the TDS analysis, considering that XPS depth-profile analysis indicates similar signals in the N 1s and C 1s peaks (Figures S8–S10), a small amount of N and C impurities keep evidently changing in the N₂O plasma reactant.

Understanding the Relationship between N and C Species Deposited Using N₂O Plasma Reactants via Theoretical Interpretation. To understand the relationship between the C and N species in the In₂O₃, Ga₂O₃, and ZnO films fabricated using the N₂O plasma reactant, DFT calculations were performed, as shown in Figure 6. Thermodynamical predictions suggest that CO or CO₂ present on the surface of reducible oxides desorbs quickly. As indicated by the TDS spectra, the DFT-calculated CO₂ desorption energies (E_{des}) from the In₂O₃, Ga₂O₃, and ZnO matrixes are all compensated by the entropic contribution to the Gibbs free energy of CO₂ desorption from the oxide surfaces at room temperature. Because the E_{des} values indicate that oxygen ions at the surfaces oxidize the residual C in the films during PEALD, CO₂ naturally desorbs, leaving V_O behind, which becomes a gateway for ON adsorption and dissociation (Figure S11). The V_O generated upon the release of C from the oxide films strengthens the ON radical binding on the In₂O₃, Ga₂O₃, and ZnO surfaces. The surface-adsorbed ON molecules on In₂O₃ and Ga₂O₃ behave in a similar manner. The ON radical spontaneously dissociated into N and O ions on the In₂O₃ and Ga₂O₃ surfaces, staying over V_O and healing them. The strong negative ΔE values presented in Figure 6b,c confirm that ON dissociation is highly thermodynamically

driven. Consequently, the dissociated N ions are well embedded in the lattices of the In₂O₃ and Ga₂O₃ films, suggesting that N ions are possibly included within these film matrices during the PEALD process. In contrast to the DFT calculation results, N was undetected in the In₂O₃ film fabricated utilizing a N₂O plasma time of 5 s because of the insufficient driving force of the ON adsorption during the short plasma time owing to the residual C-related impurities. However, the significant decrease in C-related impurities in the In₂O₃ film prepared utilizing a N₂O plasma time of 10 s can trigger the gateway for ON adsorption; therefore N can form strong bonds with indium ions. In contrast, the ΔE values of ON dissociation and V_O healing were primarily neutral on ZnO as shown in Figure 6d. Therefore, the decrease in the level of O_{def} of ZnO with increasing N₂O plasma time is attributed to V_O healing through the presence of O atoms formed by ON dissociation. Instead, the ΔE of N₂ production from a dissociated ON pair was highly negative, corroborating that the N ions were released from the ZnO film rather than penetrating the ZnO matrix. This result indicates that the experimental detection of N within ZnO films synthesized utilizing a N₂O plasma reactant is a rare event. Our DFT-based theoretical interpretation confirms that the energetics of the serial C impurity release, ON adsorption and dissociation, N embedment, and N₂ release combined and concurrently predicted whether the IGZO component diminished the intrinsic C impurities and accepted the N within the matrix.

PBTS Stability for PEALD-IGZO TFTs with Selective N₂O Plasma Reactants. To examine the relationship between the selective N₂O plasma reactant and reliability, we evaluate the negative bias temperature stress (NBTS) and PBTS stability of the IGZO TFTs fabricated by using N₂O plasma for each cation material. During the stability tests, the devices were stressed under a gate bias stress of ± 2 MV/cm for 10000 s at 95 °C. As shown in Figure S12, the devices show fairly good NBTS stability because of the low hole concentration in the oxide semiconductors. Figure 7a presents the transfer characteristics of the reference and selectively N₂O plasma-applied IGZO TFTs as a function of the PBTS time, and the extent of the V_{TH} shift after 10000 s is compared in Figure 7b. The transfer curves of the devices under the PBTS conditions are shown in Figure S13. The extent of the V_{TH} shift was degraded by 68% in the I^{*}GZO TFT compared with the reference IGZO TFT. Interestingly, the I^{*}GZO TFTs demonstrated enhanced PBTS results of up to 50% with increasing N₂O plasma time, while negligible changes were observed in the I^{*}ZnO TFTs. V_O is popularly regarded as an

important factor in determining the instability of oxide-based TFTs. In general, V_O exhibits two types of charge states: a neutral charge state (V_O^0) and a 2+ charge state (V_O^{2+}) state. The formation energy for these states relies on the Fermi energy level (E_F). During PBTS, the thermal energy accelerates the V_O state transitions involving electron traps as follows: $V_O^{2+} + 2e^- \rightarrow V_O^0$.^{3,45–48} For the I*GZO TFTs, degraded PBTS stability is assumed to originate from the generation of oxygen-related defects (interstitial oxygen or peroxide) with increasing the N_2O plasma time. However, the N content in Ga_2O_3 prepared by using the N_2O plasma reactant can trigger diminishing V_O defects, leading to a significantly improved PBTS stability in IG*ZO TFTs. Further, because of the negligible changes in the acceptor-like state in the ZnO film, the IGZ*O TFTs exhibited similar PBTS reliability. Consequently, a PEALD-IGZO TFT with an improved mobility and stability trade-off could be obtained by the N doping process in the Ga_2O_3 layers utilizing N_2O plasma reactant in its subcycles.

CONCLUSIONS²

We successfully designed high-performance PEALD-IGZO TFTs via selective N doping. The electrical characteristics of selectively controlled IGZO TFTs primarily rely on the N_2O plasma reactant for each cationic material. We discovered that the variations in oxygen-related defects and C impurities in N_2O plasma reactants greatly influence the electrical properties. In addition, the subgap states are significantly diminished only in Ga_2O_3 , which is attributed to N doping via the N_2O plasma reactant. Through a combined theoretical and experimental study, the surface defects derived from intrinsic C-related impurities were determined to behave as a gateway for N penetration into Ga_2O_3 . Owing to these beneficial effects, IGZO TFTs containing Ga_2O_3 components grown with N_2O plasma reactant exhibit high stability and reliability under harsh PBTS environments, even after possessing extremely high mobility ($106.5 \pm 2.7 \text{ cm}^2/(\text{V s})$). Our study provides insight into the proper application of N_2O plasma reactants, and this process may help advance the high-performance semiconductor field.

ASSOCIATED CONTENT⁴

Supporting Information⁵

The Supporting Information is available free of charge at <https://pubs.acs.org/doi/10.1021/acsami.3c05678>.

Comparison of device key parameters of IGZO TFT deposited using O_2 and N_2O plasma reactants, XRF-derived cation atomic composition of the IGZO films deposited using O_2 and N_2O plasma reactants, XRF-derived cation atomic composition of the three splits of IGZO films deposited using selective N_2O plasma reactant, cation atomic composition of the IGZO films, crystallinity of the IGZO deposited using selective N_2O plasma reactant, effect of N_2O plasma reactant on electrical characteristics in the In_2O_3 and ZnO films, chemical bonding status with the oxygen of the In_2O_3 , Ga_2O_3 , and ZnO films fabricated with O_2 or N_2O plasma reactant, subgap states of the In_2O_3 , Ga_2O_3 , and ZnO films deposited using O_2 or N_2O plasma reactant, surface roughness of the IGZO deposited using selective N_2O plasma reactant, desorption behaviors of the nitrogen and carbon species in the In_2O_3 , Ga_2O_3 , and ZnO films,

nitrogen and carbon distributions in the depth profiles of the In_2O_3 , Ga_2O_3 , and ZnO films, DFT-calculated energetics of carbon release, evaluation of the NBTS and PBTS stability for reference and controlled IGZO TFTs (PDF)

AUTHOR INFORMATION⁹

Corresponding Authors

Hyun You Kim – Department of Materials Science and Engineering, Chungnam National University, Daejeon 34134, Republic of Korea; orcid.org/0000-0001-8105-1640; Email: kimhy@cnu.ac.kr

Jin-Seong Park – Division of Materials Science and Engineering, Hanyang University, Seoul 04763, Republic of Korea; orcid.org/0000-0002-9070-5666; Email: jsparklime@hanyang.ac.kr

Authors¹¹

Dong-Gyu Kim – Division of Materials Science and Engineering, Hanyang University, Seoul 04763, Republic of Korea

Hyuk Choi – Department of Materials Science and Engineering, Chungnam National University, Daejeon 34134, Republic of Korea; orcid.org/0000-0002-7899-2631

Yoon-Seo Kim – Division of Materials Science and Engineering, Hanyang University, Seoul 04763, Republic of Korea

Dong-Hyeon Lee – Division of Materials Science and Engineering, Hanyang University, Seoul 04763, Republic of Korea

Hye-Jin Oh – Division of Materials Science and Engineering, Hanyang University, Seoul 04763, Republic of Korea

Ju Hyek Lee – Department of Materials Science and Engineering, Chungnam National University, Daejeon 34134, Republic of Korea

Junghwan Kim – Graduate School of Semiconductor Materials and Devices Engineering, Ulsan National Institute of Science and Technology, Ulsan 44919, Republic of Korea; orcid.org/0000-0001-9168-6260

Seunghee Lee – Semiconductor R&D Center, Samsung Electronics, Hwaseong-si, Gyeonggi-do 18448, Republic of Korea

Bongjin Kuh – Semiconductor R&D Center, Samsung Electronics, Hwaseong-si, Gyeonggi-do 18448, Republic of Korea

Taewon Kim – Semiconductor R&D Center, Samsung Electronics, Hwaseong-si, Gyeonggi-do 18448, Republic of Korea

Complete contact information is available at: [13](https://doi.org/10.1021/acsami.3c05678)

<https://pubs.acs.org/doi/10.1021/acsami.3c05678>

Author Contributions¹⁴

D.-G.K. and H.C. contributed equally to this work. D.-G.K.: concept and device fabrication, writing an original draft. H.C.: theoretical research, writing of theory section of the original draft. Y.-S.K.: device fabrication, analysis. D.-H.L.: measuring device characteristics. H.-J.O.: measuring device characteristics. J.H.L.: theoretical research. J.K.: analysis. S.L.: measuring device stability. B.K.: measuring device stability. T.K.: measuring device stability. H.Y.K.: theoretical research, editing of the original draft. J.-S.P.: concept and supervision, editing of the original draft.

Notes 1

The authors declare no competing financial interest.²

ACKNOWLEDGMENTS 3

This work was supported by Samsung Electronics Co., Ltd. (IO220405-09482-01).

REFERENCES 5

- (1) Kim, J. H.; Kang, S.; Lee, S.; Kim, H.; Ro, Y.; Lee, S.; Wang, D.; Choi, J.; So, J.; Cho, Y.; Song, J.; Cho, J.; Sohn, K.; Kim, N. S. Aquabolt-XL HBM2-PIM, LPDDR5-PIM With In-Memory Processing, and AXDIMM With Acceleration Buffer. *IEEE Micro* **2022**, *42* (3), 20–30.
- (2) Li, C.; Hu, M.; Li, Y.; Jiang, H.; Ge, N.; Montgomery, E.; Zhang, J.; Song, W.; Dávila, N.; Graves, C. E.; Li, Z.; Strachan, J. P.; Lin, P.; Wang, Z.; Barnell, M.; Wu, Q.; Williams, R. S.; Yang, J. J.; Xia, Q. Analogue Signal and Image Processing with Large Memristor Crossbars. *Nat. Electron.* **2018**, *1* (1), 52–59.
- (3) Kamiya, T.; Nomura, K.; Hosono, H. Present Status of Amorphous In-Ga-Zn-O Thin-Film Transistors. *Sci. Technol. Adv. Mater.* **2010**, *11* (4), 044305.
- (4) Kamiya, T.; Hosono, H. Material Characteristics and Applications of Transparent Amorphous Oxide Semiconductors. *NPG Asia Mater.* **2010**, *2* (1), 15–22.
- (5) Magari, Y.; Kataoka, T.; Yeh, W.; Furuta, M. High-Mobility Hydrogenated Polycrystalline In₂O₃ (In₂O₃:H) Thin-Film Transistors. *Nat. Commun.* **2022**, *13* (1), 1–8.
- (6) Si, M.; Lin, Z.; Chen, Z.; Sun, X.; Wang, H.; Ye, P. D. Scaled Indium Oxide Transistors Fabricated Using Atomic Layer Deposition. *Nat. Electron.* **2022**, *5* (3), 164–170.
- (7) Barquinha, P.; Pereira, L.; Gonçalves, G.; Kuscer, D.; Kosec, M.; Vilà, A.; Olziersky, A.; Morante, J. R.; Martins, R.; Fortunato, E. Low-Temperature Sputtered Mixtures of High- κ and High Bandgap Dielectrics for GIZO TFTs. *J. Soc. Inf. Dispersion* **2010**, *18* (10), 762–772.
- (8) Kim, H.; Im, K.; Park, J.; Khim, T.; Hwang, H.; Kim, S.; Lee, S.; Song, M.; Choi, P.; Song, J.; Choi, B. The Effects of Valence Band Offset on Threshold Voltage Shift in A-InGaZnO TFTs under Negative Bias Illumination Stress. *IEEE Electron Device Lett.* **2020**, *41* (5), 737–740.
- (9) Choi, C. H.; Kim, T.; Ueda, S.; Shiah, Y.-S.; Hosono, H.; Kim, J.; Jeong, J. K. High-Performance Indium Gallium Tin Oxide Transistors with an Al₂O₃ Gate Insulator Deposited by Atomic Layer Deposition at a Low Temperature of 150°C: Roles of Hydrogen and Excess Oxygen in the Al₂O₃ Dielectric Film. *ACS Appl. Mater. Interfaces* **2021**, *13* (24), 28451–28461.
- (10) Cho, S.-I.; Ko, J. B.; Lee, S. H.; Kim, J.; Park, S.-H. K. Remarkably Stable High Mobility Self-Aligned Oxide TFT by Investigating the Effect of Oxygen Plasma Time during PEALD of SiO₂ Gate Insulator. *J. Alloys Compd.* **2022**, *893*, 162308.
- (11) Kim, D.-G.; Yoo, K. S.; Kim, H.-M.; Park, J.-S. Impact of N₂O Plasma Reactant on PEALD-SiO₂ Insulator for Remarkably Reliable ALD-Oxide Semiconductor TFTs. *IEEE Trans. Electron Devices* **2022**, *69* (6), 3199–3205.
- (12) Nomura, K.; Kamiya, T.; Ohta, H.; Uruga, T.; Hirano, M.; Hosono, H. Local Coordination Structure and Electronic Structure of the Large Electron Mobility Amorphous Oxide Semiconductor In-Ga-Zn-O: Experiment and Ab Initio Calculations. *Phys. Rev. B - Condens. Matter Mater. Phys.* **2007**, *75* (3), 2–6.
- (13) Park, J. S.; Maeng, W.-J.; Kim, H.-S.; Park, J.-S. Review of Recent Developments in Amorphous Oxide Semiconductor Thin-Film Transistor Devices. *Thin Solid Films* **2012**, *520* (6), 1679–1693.
- (14) Luo, Y.-R. Bond Dissociation Energies. *CRC Handb. Chem. Phys.* **2012**, *89*, 89.
- (15) Yamazaki, S. Crystalline Oxide Semiconductor Using CAAC-IGZO and Its Application. *ECS Meet. Abstr.* **2014**, *64* (10), 155.
- (16) Shin, Y.; Kim, S. T.; Kim, K.; Kim, M. Y.; Oh, S.; Jeong, J. K. The Mobility Enhancement of Indium Gallium Zinc Oxide

Transistors via Low-Temperature Crystallization Using a Tantalum Catalytic Layer. *Sci. Rep.* **2017**, *7* (1), 1–10.

(17) Jeong, S.; Jang, S.; Han, H.; Kim, H.; Choi, C. C-Axis Aligned Crystalline Indium-Gallium-Zinc Oxide (CAAC-IGZO) and High-k Charge Trapping Film for Flash Memory Application. *J. Alloys Compd.* **2021**, *888*, 161440.

(18) Glushkova, A. V.; Dekkers, H. F. W.; Nag, M.; Del Agua Bornique, J. I.; Ramalingam, J.; Genoe, J.; Heremans, P.; Rolin, C. Systematic Study on the Amorphous, C-Axis-Aligned Crystalline, and Protocrystalline Phases in In-Ga-Zn Oxide Thin-Film Transistors. *ACS Appl. Electron. Mater.* **2021**, *3* (3), 1268–1278.

(19) Raja, J.; Jang, K.; Balaji, N.; Choi, W.; Thuy Trinh, T.; Yi, J. Negative Gate-Bias Temperature Stability of N-Doped InGaZnO Active-Layer Thin-Film Transistors. *Appl. Phys. Lett.* **2013**, *102* (8), 083505.

(20) Park, K.; Kim, J. H.; Sung, T.; Park, H. W.; Baeck, J. H.; Bae, J.; Park, K. S.; Yoon, S.; Kang, I.; Chung, K.-B.; Kim, H.-S.; Kwon, J.-Y. Highly Reliable Amorphous In-Ga-Zn-O Thin-Film Transistors Through the Addition of Nitrogen Doping. *IEEE Trans. Electron Devices* **2019**, *66* (1), 457–463.

(21) Raja, J.; Jang, K.; Balaji, N.; Yi, J. Suppression of Temperature Instability in InGaZnO Thin-Film Transistors by in Situ Nitrogen Doping. *Semicond. Sci. Technol.* **2013**, *28* (11), 115010.

(22) Richey, N. E.; de Paula, C.; Bent, S. F. Understanding Chemical and Physical Mechanisms in Atomic Layer Deposition. *J. Chem. Phys.* **2020**, *152* (4), 040902.

(23) Johnson, R. W.; Hultqvist, A.; Bent, S. F. A Brief Review of Atomic Layer Deposition: From Fundamentals to Applications. *Mater. Today* **2014**, *17* (5), 236–246.

(24) George, S. M. Atomic Layer Deposition: An Overview. *Chem. Rev.* **2010**, *110* (1), 111–131.

(25) Cho, M. H.; Choi, C. H.; Jeong, J. K. Comparative Study of Atomic Layer Deposited Indium-Based Oxide Transistors with a Fermi Energy Level-Engineered Heterojunction Structure Channel through a Cation Combinatorial Approach. *ACS Appl. Mater. Interfaces* **2022**, *14* (16), 18646–18661.

(26) Sheng, J.; Hong, T. H.; Lee, H.-M.; Kim, K. R.; Sasase, M.; Kim, J.; Hosono, H.; Park, J.-S. Amorphous IGZO TFT with High Mobility of 70 Cm²/(V s) via Vertical Dimension Control Using PEALD. *ACS Appl. Mater. Interfaces* **2019**, *11* (43), 40300–40309.

(27) Cho, M. H.; Choi, C. H.; Seul, H. J.; Cho, H. C.; Jeong, J. K. Achieving a Low-Voltage, High-Mobility IGZO Transistor through an ALD-Derived Bilayer Channel and a Hafnia-Based Gate Dielectric Stack. *ACS Appl. Mater. Interfaces* **2021**, *13* (14), 16628–16640.

(28) Yoo, K. S.; Kim, D.-G.; Lee, S.; Lee, W.-B.; Park, J.-S. Atmospheric Pressure Spatial ALD of Al₂O₃ Thin Films for Flexible PEALD IGZO TFT Application. *Ceram. Int.* **2022**, *48* (13), 18803–18810.

(29) Moon, S.-H.; Bae, S.-H.; Kwon, Y.-H.; Seong, N.-J.; Choi, K.-J.; Yoon, S.-M. Combination of InZnO/InGaZnO Bi-Layered Channels Prepared by Atomic Layer Deposition and Ozone-Based Gate-Stack Formation for Guaranteeing High Field-Effect Mobility and Long-Term Stability of Thin Film Transistors. *Ceram. Int.* **2022**, *48* (14), 20905–20913.

(30) Seul, H. J.; Cho, J. H.; Hur, J. S.; Cho, M. H.; Cho, M. H.; Ryu, M. T.; Jeong, J. K. Improvement in Carrier Mobility through Band-Gap Engineering in Atomic-Layer-Deposited In-Ga-Zn-O Stacks. *J. Alloys Compd.* **2022**, *903*, 163876.

(31) Lee, S.; Jeon, H. Characteristics of an Al₂O₃ Thin Film Deposited by a Plasma Enhanced Atomic Layer Deposition Method Using N₂O Plasma. *Electron. Mater. Lett.* **2007**, *3* (1), 17–21.

(32) Kim, S.; Kim, J.; Choi, J.; Kang, H.; Jeon, H.; Bae, C. Characteristics of HfO₂ Thin Films Deposited by Plasma-Enhanced Atomic Layer Deposition Using O₂ Plasma and N₂O Plasma. *J. Vac. Sci. Technol. B Microelectron. Nanom. Struct.* **2006**, *24* (3), 1088–1093.

(33) Won, S.-J.; Kim, J.-Y.; Choi, G.-J.; Heo, J.; Hwang, C. S.; Kim, H. J. The Formation of an Almost Full Atomic Monolayer via Surface Modification by N₂O-Plasma in Atomic Layer Deposition of ZrO₂ Thin Films. *Chem. Mater.* **2009**, *21* (19), 4374–4379.

- (34) Mourey, D. A.; Zhao, D. A.; Sun, J.; Jackson, T. N. Fast PEALD ZnO Thin-Film Transistor Circuits. *IEEE Trans. Electron Devices* **2010**, *57* (2), 530–534.
- (35) Kresse, G.; Furthmüller, J. Efficient Iterative Schemes for Ab Initio Total-Energy Calculations Using a Plane-Wave Basis Set. *Phys. Rev. B* **1996**, *54* (16), 11169.
- (36) Kresse, G.; Joubert, D. From Ultrasoft Pseudopotentials to the Projector Augmented-Wave Method. *Phys. Rev. B* **1999**, *59* (3), 1758.
- (37) Perdew, J. P.; Burke, K.; Wang, Y. Generalized Gradient Approximation for the Exchange-Correlation Hole of a Many-Electron System. *Phys. Rev. B - Condens. Matter Mater. Phys.* **1996**, *54* (23), 16533.
- (38) Klimeš, J.; Michaelides, A. Perspective: Advances and Challenges in Treating van Der Waals Dispersion Forces in Density Functional Theory. *J. Chem. Phys.* **2012**, *137* (12), 120901.
- (39) Blöchl, P. E. Projector Augmented-Wave Method. *Phys. Rev. B* **1994**, *50* (24), 17953.
- (40) Dudarev, S. L.; Botton, G. A.; Savrasov, S. Y.; Humphreys, C. J.; Sutton, A. P. Electron-Energy-Loss Spectra and the Structural Stability of Nickel Oxide: An LSDA+U Study. *Phys. Rev. B* **1998**, *57* (3), 1505.
- (41) Dudarev, S. L.; Botton, G. A.; Savrasov, S. Y.; Szotek, Z.; Temmerman, W. M.; Sutton, A. P. Electronic Structure and Elastic Properties of Strongly Correlated Metal Oxides from First Principles: LSDA + U, SIC-LSDA and EELS Study of UO₂ and NiO. *Phys. status solidi* **1998**, *166* (1), 429–443.
- (42) Dong, L.; Jia, R.; Xin, B.; Peng, B.; Zhang, Y. Effects of Oxygen Vacancies on the Structural and Optical Properties of β -Ga₂O₃. *Sci. Rep.* **2017**, *7* (1), 1–12.
- (43) Lee, J.-H.; Sheng, J.; An, H.; Hong, T.; Kim, H. Y.; Lee, H.; Seok, J. H.; Park, J. W.; Lim, J. H.; Park, J.-S. Metastable Rhombohedral Phase Transition of Semiconducting Indium Oxide Controlled by Thermal Atomic Layer Deposition. *Chem. Mater.* **2020**, *32* (17), 7397–7403.
- (44) Kamiya, T.; Nomura, K.; Hosono, H. Origins of High Mobility and Low Operation Voltage of Amorphous Oxide TFTs: Electronic Structure, Electron Transport, Defects and Doping. *J. Dispersion Technol.* **2009**, *5* (7), 273–288.
- (45) Ide, K.; Nomura, K.; Hosono, H.; Kamiya, T. Electronic Defects in Amorphous Oxide Semiconductors: A Review. *Phys. status solidi* **2019**, *216* (5), 1800372.
- (46) Janotti, A.; Van de Walle, C. G. Oxygen Vacancies in ZnO. *Appl. Phys. Lett.* **2005**, *87* (12), 122102.
- (47) Janotti, A.; Van de Walle, C. G. Native Point Defects in ZnO. *Phys. Rev. B* **2007**, *76* (16), 165202.
- (48) Gallino, F.; Pacchioni, G.; Di Valentin, C. Transition Levels of Defect Centers in ZnO by Hybrid Functionals and Localized Basis Set Approach. *J. Chem. Phys.* **2010**, *133* (14), 144512.
- (49) Kim, J.-S.; Joo, M.-K.; Xing Piao, M.; Ahn, S.-E.; Choi, Y.-H.; Jang, H.-K.; Kim, G.-T. Plasma Treatment Effect on Charge Carrier Concentrations and Surface Traps in A-InGaZnO Thin-Film Transistors. *J. Appl. Phys.* **2014**, *115* (11), 114503.
- (50) Sheng, J.; Park, J.; Choi, D.; Lim, J.; Park, J. S. A Study on the Electrical Properties of Atomic Layer Deposition Grown InOx on Flexible Substrates with Respect to N₂O Plasma Treatment and the Associated Thin-Film Transistor Behavior under Repetitive Mechanical Stress. *ACS Appl. Mater. Interfaces* **2016**, *8* (45), 31136–31143.
- (51) Shiah, Y.-S.; Sim, K.; Shi, Y.; Abe, K.; Ueda, S.; Sasase, M.; Kim, J.; Hosono, H. Mobility-Stability Trade-off in Oxide Thin-Film Transistors. *Nat. Electron.* **2021**, *4* (11), 800–807.
- (52) Shiah, Y.-S.; Sim, K.; Ueda, S.; Kim, J.; Hosono, H. Unintended Carbon-Related Impurity and Negative Bias Instability in High-Mobility Oxide TFTs. *IEEE Electron Device Lett.* **2021**, *42* (9), 1319–1322.